THE ASTROPHYSICAL JOURNAL, 542:453–463, 2000 October 10

THE BAR-MODE INSTABILITY IN DIFFERENTIALLY ROTATING NEUTRON STARS: SIMULATIONS IN FULL GENERAL RELATIVITY

MASARU SHIBATA,[1] THOMAS W. BAUMGARTE, AND STUART L. SHAPIRO[2]

Department of Physics, University of Illinois at Urbana-Champaign, Urbana, IL 61801

Received 2000 February 15; accepted 2000 May 19

ABSTRACT

We study the dynamical stability against bar-mode deformation of rapidly spinning neutron stars with differential rotation. We perform fully relativistic three-dimensional simulations of compact stars with $M/R \geq 0.1$, where M is the total gravitational mass and R the equatorial circumferential radius. We adopt an adiabatic equation of state with adiabatic index $\Gamma = 2$. As in Newtonian theory, we find that stars above a critical value of $\beta \equiv T/W$ (where T is the rotational kinetic energy and W the gravitational binding energy) are dynamically unstable to bar formation. For our adopted choices of stellar compaction and rotation profile, the critical value of $\beta = \beta_{\rm dGR}$ is $\sim$0.24–0.25, only slightly smaller than the well-known Newtonian value $\sim$0.27 for incompressible Maclaurin spheroids. The critical value depends only very weakly on the degree of differential rotation for the moderate range we surveyed. All unstable stars form bars on a dynamical timescale. Models with sufficiently large β subsequently form spiral arms and eject mass, driving the remnant to a dynamically stable state. Models with moderately large $\beta \gtrsim \beta_{\rm dGR}$ do not develop spiral arms or eject mass but adjust to form dynamically stable ellipsoidal-like configurations. If the bar-mode instability is triggered in supernova collapse or binary neutron star mergers, it could be a strong and observable source of gravitational waves. We determine characteristic wave amplitudes and frequencies.

Subject headings: dense matter — relativity — stars: neutron — stars: rotation

1. INTRODUCTION

Neutron stars in nature are rotating and subject to nonaxisymmetric rotational instabilities. An exact treatment of these instabilities exists only for incompressible equilibrium fluids in Newtonian gravity (see, e.g., Chandrasekhar 1969; Tassoul 1978; Shapiro & Teukolsky 1983). For these configurations, global rotational instabilities arise from nonradial toroidal modes $e^{im\varphi}$ ($m = \pm 1, \ \pm 2, \ \ldots$) when $\beta \equiv T/W$ exceeds a certain critical value. Here φ is the azimuthal coordinate, and T and W are the rotational kinetic and gravitational potential binding energies. In the following, we will focus on the $m = \pm 2$ bar mode since it is the fastest growing mode when the rotation is sufficiently rapid.

There exist two different mechanisms and corresponding timescales for bar-mode instabilities. Uniformly rotating, incompressible stars in Newtonian theory are *secularly* unstable to bar-mode formation when $\beta \geq \beta_s \simeq 0.14$. However, this instability can grow only in the presence of some dissipative mechanism, like viscosity or gravitational radiation, and the growth time is determined by the dissipative timescale, which is usually much longer than the dynamical timescale of the system. By contrast, a *dynamical* instability to bar-mode formation sets in when $\beta \geq \beta_d \simeq 0.27$. This instability is independent of any dissipative mechanisms, and the growth time is determined by the hydrodynamical timescale of the system.

The secular instability in compressible stars, both uniformly and differentially rotating, has been analyzed numerically within linear perturbation theory by means of a variational principle and trial functions, by solving the eigenvalue problem, or by other approximate means. This technique has been applied not only in Newtonian theory (Lynden-Bell & Ostriker 1967; Ostriker & Bodenheimer 1973; Imamura et al. 1985; Ipser & Lindblom 1990; Friedman & Schutz 1978) but also in post-Newtonian theory (Cutler & Lindblom 1992; see Shapiro & Zane 1998 for incompressible stars) and full general relativity (Yoshida & Eriguchi 1999; Bonazzola, Frieben, & Gourgoulhon 1996; Stergioulas & Friedman 1998). For relativistic stars, the critical value of β_s depends on the compaction M/R of the star (where M is the gravitational mass and R the circumferential radius at the equator), on the rotation law, and on the dissipative mechanism. The gravitational radiation–driven instability occurs for smaller rotation rates, i.e., for values $\beta_s < 0.14$, in general relativity. For extremely compact stars (Stergioulas & Friedman 1998) or strongly differentially rotating stars (Imamura et al. 1995), the critical value can be as small as $\beta_s < 0.1$. By contrast, viscosity drives the instability to higher rotation rates $\beta_s > 0.14$ as the configurations become more compact (Bonazzola et al. 1996; Shapiro & Zane 1998).

Determining the onset of the dynamical bar-mode instability, as well as the subsequent evolution of an unstable star, requires a numerical simulation of the fully nonlinear hydrodynamical equations. Simulations performed in Newtonian theory (e.g., Tohline, Durisen, & McCollough 1985; Durisen et al. 1986; Williams & Tohline 1987, 1988; Houser, Centrella, & Smith 1994; Smith, Houser, & Centrella 1996; Houser & Centrella 1996; Pickett, Durisen, & Davis 1996; New, Centrella, & Tohline 2000) have shown that β_d depends only very weakly on the stiffness of the equation of state. Once a bar has developed, the formation of spiral arms plays an important role in redistributing the angular momentum and forming a core-halo structure. Recently, it has been shown that, similar to the onset of secular insta-

---

[1] Department of Earth and Space Science, Graduate School of Science, Osaka University, Toyonaka, Osaka 560-0043, Japan.

[2] Department of Astronomy and NCSA, University of Illinois at Urbana-Champaign, Urbana, IL 61801.

bility, β_d can be smaller for stars with a higher degree of differential rotation (Tohline & Hachisu 1990; Pickett et al. 1996).

To date, the dynamical bar-mode instability has been analyzed only in Newtonian theory, hence, almost nothing is known about the role of relativistic gravitation. The reason is that until quite recently a stable numerical code capable of performing reliable hydrodynamic simulations in three dimensions plus time in full general relativity has not existed. Some recent developments, however, have advanced the field significantly. New formulations of the Einstein equation based on modifications of the standard $3+1$ ADM system of equations (Arnowitt, Deser, & Misner 1962) have resulted in codes that have proved to be remarkably stable over many dynamical timescales (e.g., Shibata & Nakamura 1995; Baumgarte & Shapiro 1999; Oohara & Nakamura 1999). In addition, gauge conditions that warrant longtime stable evolution for rotating and self-gravitating systems and are manageable computationally have been developed (e.g., Shibata 1999b). In this paper, we adopt the relativistic hydrodynamic implementation of Shibata (1999a) to study the onset and growth of the dynamical bar-mode instability in relativistic stars. Although this study is carried out only for a simple equation of state and rotational law, it demonstrates how, as numerical relativity in full $3+1$ matures, it is becoming more useful as a tool to solve long-standing problems in relativistic astrophysics characterized by strong gravitational fields and little or no spatial symmetry.

There are numerous evolutionary paths that may lead to the formation of rapidly rotating neutron stars with $\beta \sim 0.3$. The parameter β increases approximately as R^{-1} during stellar collapse. During supernova collapse, the core contracts from ~ 1000 to ~ 10 km, and hence β increases by about 2 orders of magnitude. Thus, even moderately rapidly rotating progenitor stars may yield rapidly rotating neutron stars that may reach the onset of dynamical instability (Bonazzola & Marck 1993; Rampp, Müller, & Ruffert 1998). Similar arguments hold for accretion-induced collapse of white dwarfs to neutron stars and for the merger of binary white dwarfs to neutron stars. In fact, recent X-ray and radio observations of supernova remnants have identified several young, isolated, rapidly rotating pulsars, suggesting that these stars may have been born with periods of several milliseconds (Marshall et al. 1998; Kaspi et al. 1998; Torii et al. 1999). These neutron stars could be the collapsed remnants of rapidly rotating progenitors.

Rapidly rotating neutron stars may naturally arise in the merger of binary neutron stars. Baumgarte, Shapiro, & Shibata (2000) have studied equilibrium configurations of differentially rotating neutron stars and found examples where the maximum allowed mass increases by a factor of about 2 due to differential rotation. This suggests that the merger of binary neutron stars could result in a "hypermassive" neutron star that has rest mass exceeding the maximum value for uniformly rotating stars. Recent hydrodynamic simulations in full general relativity indicate that such hypermassive neutron stars can indeed be produced in the merger of moderately compact neutron stars (Shibata & Uryu 2000). They show that the remnant is unlikely to exceed the onset point of dynamical instability initially. Subsequent neutrino emission and cooling, however, will make the star shrink in size, leading to an increase in β, possibly beyond the onset of nonradial dynamical instability, β_d.

Rapidly rotating neutron stars experiencing the bar-mode instability could have significant observable consequences. According to Newtonian simulations (Tohline et al. 1985; Durisen et al. 1986; Williams & Tohline 1987, 1988; Houser et al. 1994; Smith et al. 1996; Houser & Centrella 1996), a dynamically unstable star may evolve into a two-component system containing a central star and circumstellar accretion disk. Such a system may be observable in a supernova remnant. In the case of merged binaries, the differentially rotating remnant may be more massive, hot, and bloated than a typical rapidly rotating, old pulsar. Consequently, the frequency of gravitational waves excited by the bar-mode instability could be low, i.e., less than 1 kHz (see eq. [20] below), and hence detectable by kilometer-size laser interferometers such as Laser Interferometer Gravitational-wave Observatory (LIGO) (Lai & Shapiro 1995; Thorne 1995).

In this paper, we summarize the results of our fully relativistic simulations of bar-mode instabilities in neutron stars. We determine β_d for highly relativistic stars, follow the growth of the bar mode, and find the frequency and amplitude of the emitted gravitational waves. We implement the numerical scheme described in Shibata (1999a), using differentially rotating neutron stars of high β for initial data. We focus on differentially rotating stars since uniformly rotating stars do not reach $\beta \gtrsim 0.2$ except for extremely stiff equations of state and hence do not become dynamically unstable to bar modes (Tassoul 1978). We adopt an adiabatic equation of state with $\Gamma = 2$ as a reasonable qualitative approximation to a moderately stiff nuclear equation of state. The adiabatic assumption is justified even for hot neutron stars since energy dissipation is small over the dynamical timescales of interest.

In § 2, we briefly summarize our formulation of the fully relativistic system of equations and our numerical scheme. In § 3, initial models of differentially rotating, equilibrium neutron stars are presented. Following Shibata, Baumgarte, & Shapiro (2000), we adopt the so-called conformal flatness approximation to prepare differentially rotating neutron stars in (approximate) equilibrium states for computational convenience. To confirm the reliability of this approximation, we also compute numerically exact equilibrium states and demonstrate that this approximation is accurate (cf. Cook, Shapiro, & Teukolsky 1996). In § 4, we present our numerical results, focusing on the onset of the bar-mode instability, its early growth, and corresponding waveforms and frequencies. We briefly summarize our results in § 5.

Throughout this paper, we adopt geometrized units with $G = 1 = c$, where G and c denote the gravitational constant and speed of light, respectively. In numerical simulation, we use Cartesian coordinates $x^k = (x, y, z)$ with $r = (x^2 + y^2 + z^2)^{1/2}$, $\varpi = (x^2 + y^2)^{1/2}$, and $\varphi = \tan^{-1}(y/x)$; t denotes coordinate time. Greek indices $\mu, \nu, \ldots$ denote x, y, z, and t, and Latin indices $i, j, k, \ldots$ denote x, y, and z.

2. SUMMARY OF THE FORMULATION

We perform hydrodynamic simulations in full $3+1$ general relativity (GR). We use the same formulation and gauge conditions as in Shibata (1999a), to which the reader may refer for details and basic equations. The fundamental variables used in this paper are as follows:

$\rho =$ rest mass density ,

$\epsilon =$ specific internal energy ,

$P =$ pressure ,

$u^\mu =$ four-velocity ,

$v^k = \frac{u^k}{u^0}, \quad \Omega = v^\varphi ,$

$\alpha =$ lapse function ,

$\beta^k =$ shift vector ,

$\gamma_{ij} =$ metric in three-dimensional spatial hypersurface ,

$\gamma = e^{12\phi} = \det(\gamma_{ij}) ,$

$\tilde{\gamma}_{ij} = e^{-4\phi}\gamma_{ij} ,$

$K_{ij} =$ extrinsic curvature .

Geometric variables, ϕ, $\tilde{\gamma}_{ij}$, the trace of the extrinsic curvature $K \equiv K_{ij}\gamma^{ij}$, $\tilde{A}_{ij} \equiv e^{-4\phi}(K_{ij} - \gamma_{ij}K/3)$, as well as three auxiliary functions $F_i \equiv \partial_j \tilde{\gamma}_{ij}$, where ∂_j is the partial derivative, are evolved with an unconstrained evolution code in a modified form of the ADM formalism (Shibata & Nakamura 1995). GR hydrodynamic equations are evolved using a van Leer scheme for the advection terms (van Leer 1977; Hawley, Smarr, & Wilson 1984). Numerical simulation is performed using Cartesian coordinates. Violations of the Hamiltonian constraint and conservation of mass and angular momentum are monitored as code checks. Several test calculations, including spherical collapse of dust, stability of spherical neutron stars, and the stable evolutions of rigidly and rapidly rotating neutron stars have been described in Shibata (1999a). Simulations using this code and exploring the dynamical (quasi-radial) stability against gravitational collapse of rigidly rotating "supramassive" neutron stars, which have rest masses exceeding the maximum value for a nonrotating spherical star, have been presented in Shibata, Baumgarte, & Shapiro (2000). A simulation using this code and demonstrating the existence of dynamically stable, differentially rotating "hypermassive" stars, which have rest masses exceeding the maximum value for uniformly rotating stars, was presented in Baumgarte et al. (2000).

The stress energy tensor for an ideal fluid is given by

$$T_{\mu\nu} = (\rho + \rho\epsilon + P)u_\mu u_\nu + P g_{\mu\nu} , \tag{1}$$

where $g_{\mu\nu}$ is the spacetime metric. We adopt a Γ-law equation of state

$$P = (\Gamma - 1)\rho\epsilon , \tag{2}$$

where Γ is the adiabatic constant. For isentropic configurations, the Γ-law equation of state can be rewritten in the polytropic form

$$P = \kappa\rho^\Gamma, \quad \Gamma = 1 + \frac{1}{n} , \tag{3}$$

where κ is the polytropic constant and n the polytropic index. This is the form that we use for constructing initial data. Throughout this paper, we adopt $n = 1$ as a reasonable qualitative approximation to a moderately stiff, nuclear equation of state for simplicity.

Instead of ρ and ϵ, we numerically evolve the densities $\rho_* \equiv \rho\alpha u^0 e^{6\phi}$ and $e_* \equiv (\rho\epsilon)^{1/\Gamma}\alpha u^0 e^{6\phi}$ as the hydrodynamic variables (Shibata, Oohara, & Nakamura 1997; Shibata 1999a). Since these variables satisfy evolution equations in conservation form, the total rest mass of the system

$$M_0 = \int d^3x \rho_* \tag{4}$$

is automatically conserved, as is the volume integral of the energy density e_* in the absence of shocks.

The time-slicing and spatial gauge conditions we use in this paper for the lapse and shift are the same as those adopted in our series of papers (Shibata 1999a, 1999b; Shibata et al. 2000); i.e., we impose an "approximate" maximal slice condition ($K \simeq 0$) and an "approximate" minimum distortion gauge condition [$\tilde{D}_i(\partial_t \tilde{\gamma}^{ij}) \simeq 0$, where $\tilde{D}_i$ is the covariant derivative with respect to $\tilde{\gamma}_{ij}$; see Shibata 1999b].

3. INITIAL CONDITIONS FOR ROTATING NEUTRON STARS

As initial conditions, we adopt rapidly and differentially rotating neutron stars in (approximate) equilibrium states. The approximate equilibrium states are obtained by choosing a conformally flat spatial metric, i.e., assuming $\gamma_{ij} = e^{4\phi}\delta_{ij}$ (see, e.g., Cook et al. 1996 or Shibata 1999a for the equations to be solved in this approximate framework). This approach is computationally convenient and, as demonstrated in Cook et al. (1996) and Shibata et al. (2000), provides an excellent approximation to exact axisymmetric equilibrium configurations in rigid rotation.

Following previous studies (e.g., Komatsu, Eriguchi, & Hachisu 1989a, 1989b; Cook, Shapiro, & Teukolsky 1992, 1994; Bonazzola et al. 1993; Salgado et al. 1994; Goussard, Haensel, & Zdunik 1998), we fix the differentially rotational profile according to

$$F(\Omega) \equiv u^0 u_\varphi = A^2(\Omega_0 - \Omega) , \tag{5}$$

where A is an arbitrary constant with dimensions of length (which describes the length scale over which Ω changes) and Ω_0 is the angular velocity on the rotation axis, which is chosen to be the z-axis. In the Newtonian limit $u^0 \to 1$ and $u_\varphi \to \varpi^2\Omega$, the rotational profile reduces to

$$\Omega = \frac{A^2\Omega_0}{\varpi^2 + A^2} . \tag{6}$$

Thus, for smaller A, Ω becomes a steeper function of ϖ.

Equilibrium configurations of rotating stars are characterized by their gravitational mass M, angular momentum J, rotational kinetic energy T, and gravitational potential binding energy W, which in GR can be defined invariantly according to

$$M = \int (-2T^0_0 + T^\mu_\mu)\alpha e^{6\phi} d^3x , \tag{7}$$

$$J = \int T^0_\varphi \alpha e^{6\phi} d^3x , \tag{8}$$

$$T = \tfrac{1}{2}\int \Omega T^0_\varphi \alpha e^{6\phi} d^3x , \tag{9}$$

$$W = \int \rho_* \epsilon d^3x + T + M_0 - M \tag{10}$$

(e.g., Cook et al. 1992). For approximate configurations derived in the conformal flatness approximation, on the other hand, the gravitational mass is computed from the asymptotic behavior of the conformal factor, which, after using Gauss's law and the Hamiltonian constraint, yields

$$M = \int \left[(\rho + \rho\epsilon + P)(\alpha u^0)^2 - P + \frac{1}{16\pi} K^{ij} K_{ij} \right] \alpha e^{5\phi} \, d^3x \tag{11}$$

(see, e.g., Bowen & York 1980). This expression is correct independent of axisymmetry. For conformally flat configurations, J, T, and W can be computed from equations (8)–(10) for nonaxisymmetric configurations as well. As in Newtonian gravity, we define β as the ratio T/W. (Note $W > 0$ in our definition.)

Physical units enter the problem only through the polytropic constant κ, which can be chosen arbitrarily or else completely scaled out of the problem. In the following, we define

$$\begin{aligned} \bar{M}_0 &= M_0 \kappa^{-n/2}, \quad \bar{M} = M \kappa^{-n/2}, \\ \bar{J} &= J \kappa^{-n}, \quad \bar{P}_{\rm rot} = P_{\rm rot} \kappa^{-n/2}, \\ \bar{\rho}_{\max} &= \rho_{\max} \kappa^{n}, \end{aligned} \tag{12}$$

where $P_{\rm rot}$ and $\rho_{\max}$ are rotational period and the maximum density, respectively. Note that $\rho_{\max}$ does not necessarily coincide with the central density for stars of highly differential rotation. The barred quantities are now independent of κ, and all results can be scaled for arbitrary κ using equations (12).

For the construction of (approximate) equilibrium models for initial data, we adopt a grid in which the semimajor axes of the stars, chosen along the x- and y-axes in the equatorial plane, are covered with 40 grid points. The semiminor axis in the polar direction along the z-axis is covered with ~ 10 grid points for the case $\beta \sim 0.25$ and $A \sim r_e$. Hereafter, the coordinate lengths of the semimajor and semiminor axes are referred to as r_e and r_p, respectively. We have confirmed the convergence of our numerical solutions by increasing the number of grid points covering r_e to 120 for typical models shown in Table 1. Comparing with these higher resolution models shows that the numerical error in M, T, W, and J of the lower resolution models is less than 1%.

We find that for $n = 1$, stars with $\beta \gtrsim 0.2$ can only be constructed for $A \lesssim r_e$. Also, for $A \lesssim r_e/2$, stars with $\beta \gtrsim 0.25$ are not spheroids but toroids. Focusing on spheroidal stars with $\beta \gtrsim 0.2$, we study cases with $\hat{A} \equiv A/r_e = 0.8$ and 1.

In Table 1, we display parameters for selected models constructed both within the conformal flatness approximation and from the exact numerical equations (using the code from Cook et al. 1994) for a given $\bar{\rho}_{\max}$, $\hat{A}$, and r_p/r_e. Note that both approaches lead to valid, fully relativistic initial data in the sense that both data satisfy the constraint equations of Einstein's field equations. The difference is that the "exact" solutions provide an exactly stationary solution while the conformally flat solutions may only be approximately stationary when evolved dynamically. Here we choose stars of $R/M \sim 7$ and 9.5 (hereafter, R denotes the circumferential radius of the equator). All the stars in Table 1 are "hypermassive" (Baumgarte et al. 2000) with rest masses larger than the maximum rest mass of rigidly rotating stars built from the same equation of state ($\bar{M}_0 \simeq 0.207$; cf. Fig. 2). The matter profiles of the equilibrium configurations obtained in the conformal flatness approximation agree fairly well with the exact numerical solution. The slight deviation arises mainly from the error associated with the conformal flatness approximation (as opposed to errors due to the different finite differencing in the two distinct codes). As can be seen in Table 1, β is systematically underestimated in the conformal flatness approximation by $\lesssim 0.004$ (i.e., $\lesssim 2\%$), although the deviation for M_0 and M is considerably less ($< 1\%$ error). From a post-Newtonian point of view, T and W are quantities of $O(c^{-2})$ but M_0 and M are of $O(c^0)$. In the conformal flatness approximation, we neglect the second post-Newtonian terms of $O(c^{-4})$ in the metric (cf. Kley & Schäfer 1999) so that the error for T and W can be larger than that for masses by $O(c^2)$.[3] Indeed, the

TABLE 1

Parameters for Selected Models

r_p/r_e	$\hat{A}$	$\bar{\rho}_{\max}$	$\bar{M}_0$	$\bar{M}$	R/M	T/W	$\bar{P}^a_{\rm rot}$	$\bar{P}^e_{\rm rot}$	Stability	Model
0.35	1	0.06056	0.260	0.241	6.62	0.230	12.7	36.7	Stable	D1
			0.259	0.241	6.61	0.233	12.7			
0.275......	1	0.04460	0.277	0.259	7.07	0.258	15.0	41.8	Unstable	D2
			0.277	0.258	7.08	0.262	14.9			
0.30	1	0.04590	0.264	0.246	7.24	0.251	14.9	41.3	Unstable	D3
			0.264	0.246	7.23	0.254	14.8			
0.25	0.8	0.04650	0.262	0.245	7.02	0.243	12.3	45.3	Unstable	D4
			0.261	0.244	7.02	0.247	12.2			
0.325......	0.8	0.05940	0.254	0.235	6.50	0.223	10.5	40.2	Stable	D5
			0.253	0.235	6.50	0.226	10.4			
0.275......	1	0.03070	0.229	0.217	9.27	0.262	19.8	50.7	Unstable	D6
			0.229	0.217	9.27	0.265	19.8			
0.3	1	0.03220	0.219	0.208	9.41	0.254	19.5	49.7	Unstable	D7
			0.219	0.208	9.39	0.256	19.4			

Notes.—Maximum density $\bar{\rho}_{\max}$, rest mass $\bar{M}_0$, gravitational mass $\bar{M}$, compaction R/M, $\beta = T/W$, rotation period on the rotation axis $\varpi = 0$ ($\bar{P}^a_{\rm rot}$) and at the equator ($\bar{P}^e_{\rm rot}$) of differentially rotating stars for selected models computed in the conformally flatness approximation (upper line) and in the exact equations (lower line). For D1–D5, $R/M \sim 7$ and for D6 and D7 $R/M \sim 9.5$. For the models shown here, J/M^2 is larger than unity.

---

[3] In the conformal flatness approximation, the error in T and W is $O(c^{-4})$ and $O(c^{-6})$ in M and M_0 (see, e.g., Asada & Shibata 1996). Hence, the magnitude of the error for T and W is expected to be $\sim(GM/Rc^2)^2 \sim 2\%$ for $R/M = 7$, but that for M and M_0 is $\sim(GM/Rc^2)^3 < 1\%$, which is consistent with our numerical results.

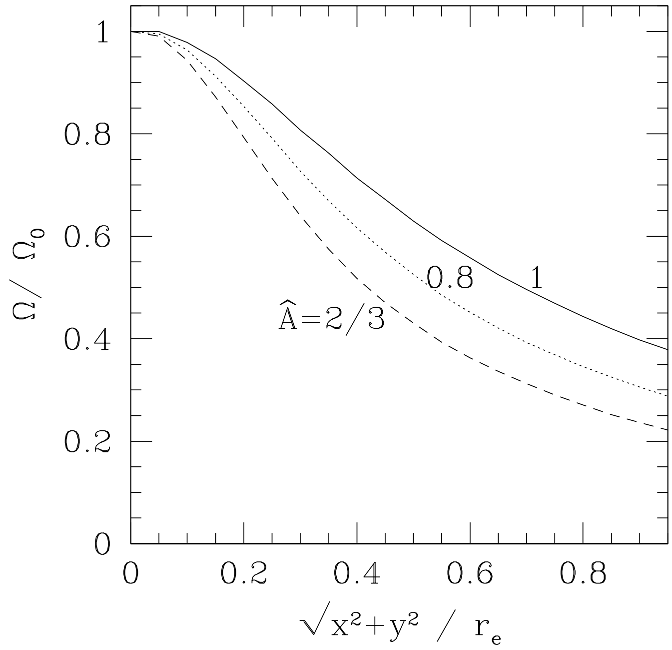

FIG. 1.—Ω/Ω_0 as a function of ϖ in the equatorial plane for differentially rotating stars of $R/M \sim 7$ and $\beta \sim \beta_{\rm dGR}$ and for $\hat{A} = 1, 0.8$, and $\frac{2}{3}$.

agreement between exact and approximate solutions is improved for less compact stars (compare models D2 and D3 with D6 and D7). Because of this small deviation from the exact solution, the initial conditions prepared in the conformal flatness approximation should be regarded as slightly perturbed states of exact equilibria.

In Figure 1, we plot Ω/Ω_0 as a function of ϖ in the equatorial plane to illustrate the rotational velocity field for different $\hat{A}$. We show an unstable (to bar modes) star with $R/M \sim 7$ and $\beta \sim 0.25$, for both $\hat{A} = 1$ and 0.8. As expected from equation (6), Ω is a steeper function of ϖ for smaller $\hat{A}$. As demonstrated in the Newtonian calculations of Pickett et al. (1996), the degree of falloff of Ω versus ϖ could be an important factor for determining the onset point of nonaxisymmetric dynamical instability in differentially rotating stars.

4. NUMERICAL RESULTS

To investigate the dynamical stability against bar-mode deformation, we initially superimpose a density perturbation of the form

$$\rho = \rho_0\left(1 + \delta_b \frac{x^2 - y^2}{r_e^2}\right), \tag{13}$$

where ρ_0 denotes the axisymmetric configuration, and we choose δ_b to be 0.1 or 0.3. We leave the four-velocity u_i unperturbed. We recompute the constraint (initial value) equations whenever we modify the equilibrium configurations this way to guarantee that we are satisfying the Einstein equations at $t = 0$.

The growth of a bar mode can be followed by monitoring the distortion parameter

$$\eta \equiv 2\,\frac{x_{\rm rms} - y_{\rm rms}}{x_{\rm rms} + y_{\rm rms}}, \tag{14}$$

where $x^i_{\rm rms}$ denotes the mean square axial length

$$x^i_{\rm rms} = \left[\frac{1}{M_0}\int d^3x \rho_*(x^i)^2\right]^{1/2}. \tag{15}$$

For dynamically unstable stars, η grows exponentially until reaching a saturation point, while for stable stars it remains approximately constant for many rotational periods.

We perform simulations using a fixed uniform grid with typical size 153 × 77 × 77 in x-y-z and assume π-rotation symmetry around the z-axis as well as a reflection symmetry about the $z = 0$ plane. We have also performed test simulations with different grid resolutions to check that the results do not change significantly. Since we impose π-rotation symmetry, we ignore one-armed spiral ($m = 1$) modes that might be dominant for rotating stars in which Ω is a very steep function of ϖ (Pickett et al. 1996). However, π-rotation symmetry guarantees that the center-of-mass drift is identically zero (cf. New et al. 2000).

We note that the outer boundaries of our computational domain reside inside the wavelength of gravitational waves emitted by the bar-mode perturbation, $\lambda_{\rm gw}$. The typical location of the outer boundaries along each axis is $\sim(0.1\text{–}0.2)\lambda_{\rm gw}$. Without setting the boundaries in the radiation zone at $r \gtrsim \lambda_{\rm gw}$, or using a sophisticated wave-extraction technique in the near zone (Bishop et al. 1996; Abrahams et al. 1998), it is impossible to compute the radiation reaction and asymptotic waveforms completely accurately. However, in this paper we focus on dynamical instabilities, which are independent of dissipation processes and grow on a dynamical timescale considerably shorter than the secular dissipation timescale due to gravitational wave emission. The error in the evaluation of the gravitational waves can therefore be safely neglected in assessing the onset and growth of a dynamical instability.

Figure 2 summarizes our findings on the dynamical stability against bar-mode deformation. We evolve a range of stellar models with $\hat{A} = 0.8$ (*squares*) and $\hat{A} = 1$ (*circles*). All of these models have $\beta \geq 0.2$ and $0.2 < r_p/r_e < 0.35$, and we determine their stability by inducing an initial nonaxisymmetric perturbation $\delta_b = 0.1$. Each model takes 50–100 CPU hr to run on the FACOM VX/4R machine; the longtime runs described below take about 150 CPU hr. Stable stars are denoted with open circles and squares and unstable stars with solid circles or squares. For models denoted by crosses, we were unable to determine stability unambiguously. Note that all differentially rotating stars shown here are dynamically stable against quasi-radial collapse to black holes.

Figure 2 shows that in an $\bar{M}_0$ versus $\bar{\rho}_{\rm max}$ diagram an unstable region can be clearly separated from a stable region. The demarcation line is nearly independent of the degree of differential rotation, at least for the modest variation in the rotation law that we consider (recall that for $\beta \gtrsim 0.2$ spheroidal stars exist only within a restricted range of $\hat{A}$). The two regions are separated by a thick dash-dotted line in the figure. We have also plotted lines of constant β: one where $\beta = 0.245$ for $\hat{A} = 1$ and another where $\beta = 0.24$ for $\hat{A} = 0.8$. These two lines very closely trace the demarcation line between the regions of stability and instability. This result suggests that *in general relativity as in Newtonian gravitation, the parameter β is a good diagnostic for assessing whether a rotating star is stable against the dynamical bar-mode instability.* It also suggests that for differentially rotat-

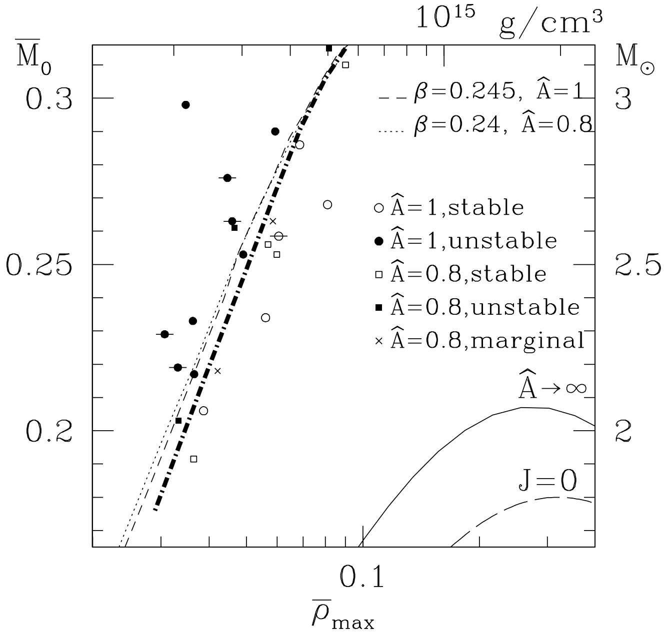

FIG. 2.—Models of differentially rotating stars in an $\bar{M}_0$ vs. $\bar{\rho}_{\max}$ diagram. Circles denote stars with $\hat{A} = 1$, squares with $\hat{A} = 0.8$. Solid (open) circles or squares represent stars that are unstable (stable). Marginally stable stars are denoted with a cross. The region for the stable stars is clearly separated from that for the unstable stars by the thick dash-dotted line. This line is followed fairly closely by the dashed and dotted lines, which have been constructed for differentially rotating stars of $(\hat{A}, \beta) =$ (1, 0.245) and (0.8, 0.24). We carry out long-duration simulations for those stars denoted by a hyphen (models D1, D2, D3, D6, and D7). The long-dashed and solid lines are for nonrotating spherical stars and rigidly rotating stars at the mass shedding limit. Scales for the top and right axes are shown for $\kappa = 100(G^3M_\odot^2/c^4)$ in which the maximum rest mass for spherical stars is about 1.8 $M_\odot$.

ing, relativistic stellar models the threshold for dynamical bar formation $\beta_{\rm dGR}$ may depend only weakly on the differential rotation law and is only slightly smaller than the corresponding value for uniformly rotating, Newtonian stars, $\beta_d \sim 0.27$.

The small but measurable decrease in the critical value of β could be due to either the presence of differential rotation (cf. Tohline & Hachisu 1990 and Pickett et al. 1996, who have observed this effect in Newtonian gravity) or GR effects (compare with the decrease in β_s with increasing compaction for the secular onset of the gravitational wave–driven instability in Stergioulas & Friedman 1998) or a combination of both. In order to separate the two effects, it would be desirable to systematically explore parameter space and study models with different rotation laws and varying compaction up to the Newtonian limit of small M/R. We are preparing such a survey now (Saijo et al. 2000).

In anticipation of this survey, recall that in Newtonian gravity $\bar{M}_0$ scales with $\bar{\rho}_{\max}^{(3-n)/2n}$ (Shapiro & Teukolsky 1983) for polytropes, or $\bar{M}_0 \propto \bar{\rho}_{\max}$ for $n = 1$. For stars with $\beta \simeq 0.27$, this relation turns out to be $\bar{M}_0 \simeq (10\text{–}12)\bar{\rho}_{\max}$; for smaller values of β, the coefficient is only slightly smaller. We therefore expect that the line marking the onset of dynamical instability, a line of constant β, approaches a linear relationship in Figure 2 in the Newtonian limit.

Unfortunately, using a fully relativistic code is impractical for simulating stars in the Newtonian or post-Newtonian regime. The Courant condition restricts the numerical time step to the light travel time across a grid zone and therefore scales with R. The dynamical timescale of the star, however, is approximately the free-fall timescale $R^{3/2}/M^{1/2}$, so that the ratio between the dynamical timescale and Courant time step scales roughly as $(R/M)^{1/2}$. In the Newtonian limit, this ratio becomes very large, so that many time steps have to be carried out in order to simulate a fixed number of dynamical timescales, which makes the calculation computationally impractical. To avoid this problem, we are implementing a post-Newtonian code (Shibata, Baumgarte, & Shapiro 1998) to explore the intermediary regime and will present these results in a forthcoming paper (Saijo et al. 2000). Our preliminary finding is that in the Newtonian limit $\beta_d \sim 0.26$ for $\hat{A} = 1$, and hence the onset of dynamical instability occurs slightly earlier for stars of greater compaction.

For five of the above models (D1, D2, D3, D6, and D7), we have followed the growth and evolution of the bar-mode instability over several rotational timescales. In Figures 3, 4, and 5, we show snapshots of density contours and velocity fields in the *x*-*y* (*left*) and *x*-*z* (*right*) planes for the compact models D1, D2, and D3 ($R/M \sim 7$; see Table 1). The models are rotating counterclockwise. Note that the stars start out as highly flattened, disklike objects. In Figure 6, we also show η as a function of time (*a*) for models D1, D2, and D3 as well as (*b*) for models D6 and D7, which are slightly less compact ($R/M \sim 9.5$). In order to accelerate the growth of the instabilities, we set $\delta_b = 0.3$ for these simulations. In addition, we plot the early evolution of $|\eta|$ on a semilog scale in Figure 7. This plot also demonstrates that while the perturbation parameter $\delta_b = 0.3$ is fairly large, the nondimensional measure $|\eta|$ is initially safely in the linear regime. Unstable growth ceases once the bar-mode reaches nonlinear saturation. Following the evolution much beyond this point is impractical, both because of accumulation of numerical error and because further evolution begins to be affected by gravitational wave emission, which is crudely handled in this code as discussed above.

Model D1 is stable against bar-mode formation and demonstrates the ability of our code to identify and maintain such a configuration in stable equilibrium (see Fig. 3). The other four models are unstable and the barlike perturbation (and hence η) grows exponentially in the early phase until saturation is reached, typically when $\eta \sim 0.2$–0.4. However, the evolution after the saturation varies for different models. For model D2, spiral arms form in the outer part of the barlike object, which then spread outward, transporting away mass and angular momentum (see Fig. 4). In Figure 8, we show the fraction of the rest mass inside a fixed coordinate radius r, $M_*(r)/M_*$, as a function of time for model D2. We find that a few percent of the total rest mass is ejected from the star. We also find that the fraction of the rest mass inside $r = 0.2r_e$ and $0.6r_e$ ultimately *increases* during the late phase of the evolution since the mass with high specific angular momentum is transported outward, and the star slightly contracts. As a consequence, the maximum density of the star increases at late times by about 50% from $\bar{\rho}_{\max} \simeq 0.045$ to ~ 0.065 by $t = 6P_{\rm rot}^a$.[4] Here

---

[4] For the stable model D1, we find a small increase in the central density as well but only by about 10% after $t = 6P_{\rm rot}^a$. This small increase is due to numerical viscosity and is a numerical artifact. The central density in the model D2 increases by a much larger fraction over the same timescale, suggesting that the bulk of this increase is indeed a physical effect.

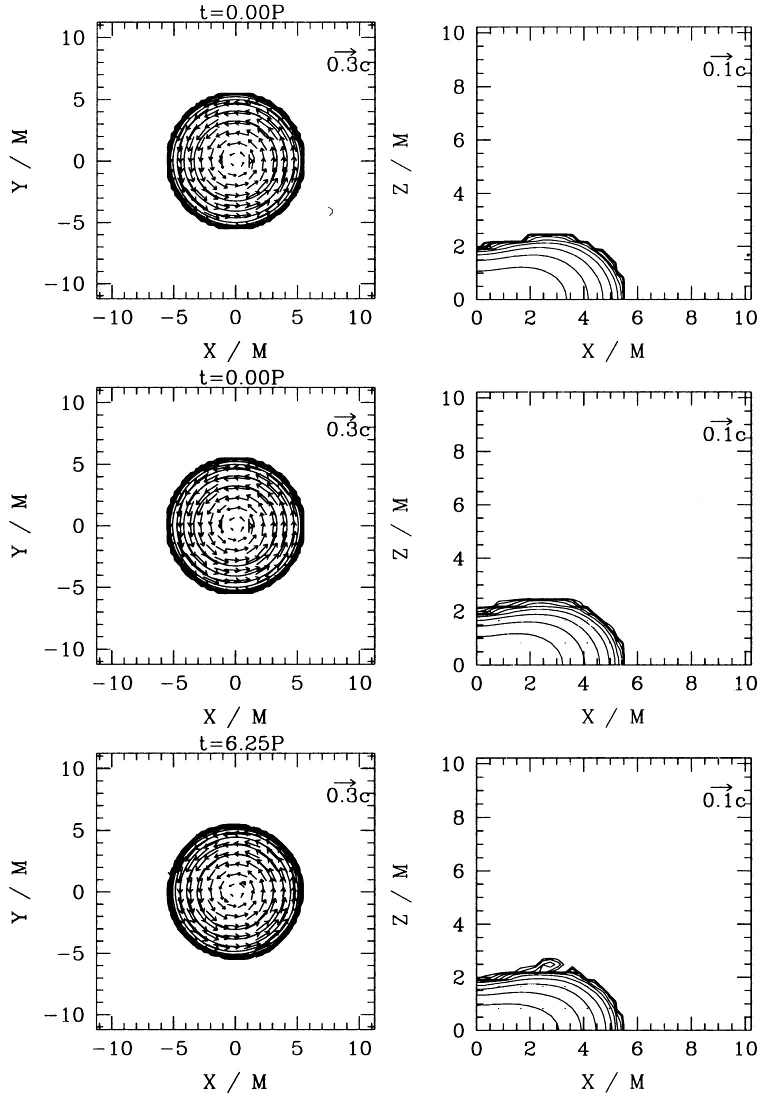

FIG. 3.—Snapshots of density contours for ρ_* and the velocity flow for v^i in the equatorial plane (*left*) and in the $y = 0$ plane (*right*) for the stable model D1. The contour lines are drawn for $\rho_*/\rho_{*\mathrm{max}} = 10^{-0.3j}$ for $j = 0, 1, 2, \ldots, 10$, where $\bar{\rho}_{*\mathrm{max}}$ is 0.193, 0.209, and 0.248 for the three different times (the corresponding values of $\bar{\rho}_{\mathrm{max}}$ are 0.061, 0.064, and 0.067). The lengths of arrows are normalized to 0.3c (*left*) and 0.1c (*right*). The time is shown in units of P^a_{rot}.

P^a_{rot} is the rotational period on the rotation axis ($\varpi = 0$). Tracking its motion in Figure 2, we find that the unstable star approaches the stability threshold line from the left and ultimately enters the stable region. Model D6 evolves very similarly. These findings are also in qualitative agreement with Newtonian results (Tohline et al. 1985; Durisen et al. 1986; Williams & Tohline 1988; Houser et al. 1994; Smith et al. 1996; Houser & Centrella 1996; New et al. 2000).

Unstable models D3 (see Fig. 5) and D7 start out closer to the stability threshold ($\beta \gtrsim \beta_{\mathrm{dGR}}$) and never form spiral arms or eject mass. Instead, they evolve to an ellipsoidal shape, which is maintained for many rotational periods. Although the mass is not ejected in this case, the maximum density slightly increases again due to outward angular momentum transport. Consequently, the stars again approach the threshold line of the dynamical stability shown in Figure 2 and become stable.

We determine the growth time and oscillation period of the bar-mode instability from Figures 7 and summarize the results in Table 2. From Figures 7, we can match η to a function

$$\eta \simeq \eta_0 \, 10^{t/\tau_g} \cos\,(2\pi t/\tau_o + \varphi_0) \,, \tag{16}$$

where η_0 and φ_0 are constants and τ_g and τ_o are the growth time and oscillation period. The growth time τ_g depends

TABLE 2

GROWTH TIME τ_g AND OSCILLATION PERIOD τ_o OF THE BAR MODE FOR UNSTABLE STARS D2, D3, D6, AND D7

Model	τ_g	τ_o
D2......	2.48	1.21
D3......	3.62	1.19
D6......	2.07	1.23
D7......	2.85	1.21

NOTE.—The timescales are shown in units of P^a_{rot}.

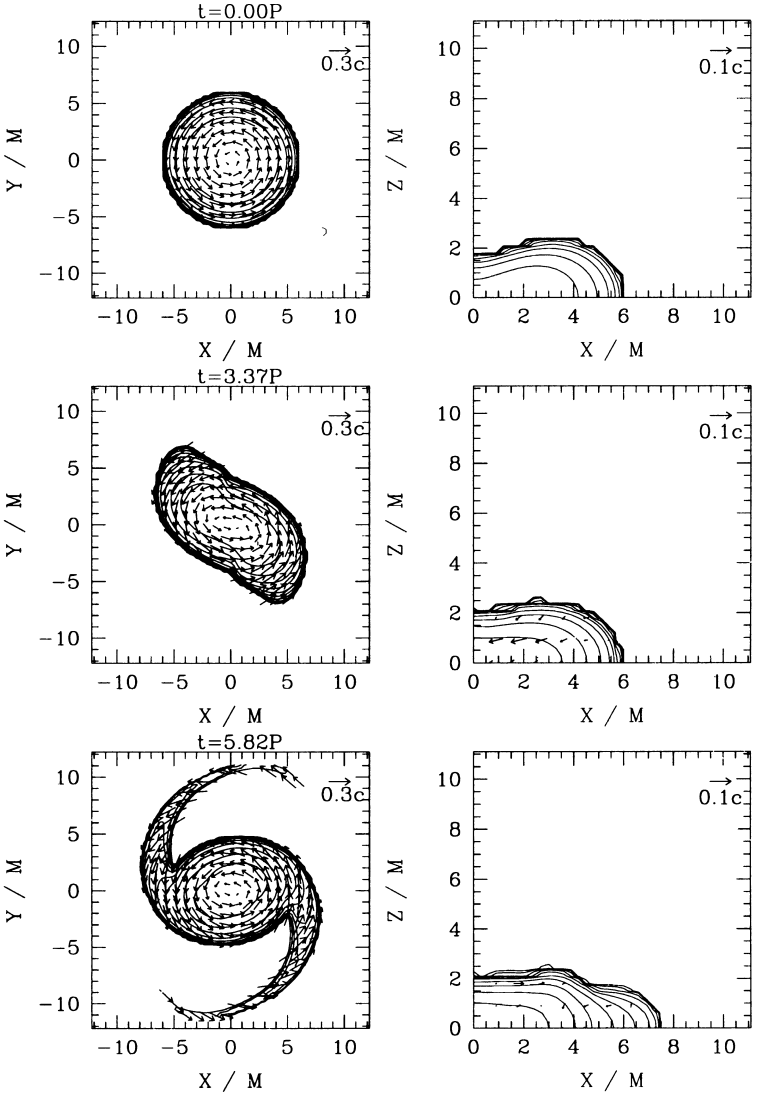

FIG. 4.—Snapshots of density contours for ρ_* and the velocity flow for v^i in the equatorial plane (*left*) and in the $y = 0$ plane (*right*) for the unstable model D2. The contour lines are drawn for $\rho_*/\rho_{*\max} = 10^{-0.3j}$ for $j = 0, 1, 2, \ldots, 10$, where $\bar{\rho}_{*\max}$ is 0.126, 0.172, and 0.264 for the three different times (the corresponding values of $\bar{\rho}_{\max}$ are 0.045, 0.059, and 0.065). The lengths of arrows are normalized to 0.3c (*left*) and 0.1c (*right*). The time is shown in units of $P^a_{\rm rot}$.

strongly on the compaction R/M and β, and τ_g is smaller for larger β as expected. The oscillation period $\tau_o \simeq 1.2P^a_{\rm rot}$ depends only very weakly on the compaction R/M and β and approximately agrees with that found in Newtonian simulations for $n = 1$ (Williams & Tohline 1988). The characteristic oscillation period of η after the saturation of the growth is $\tau_o \sim (1.2\text{–}1.4)P^a_{\rm rot}$ for all models, so that the pattern period is $\sim(2.4\text{–}2.8)P^a_{\rm rot}$.

In order to check the numerical convergence of our results, we repeated these simulations with a lower resolution (101 × 51 × 51 as opposed to 153 × 77 × 77, with the outer boundaries at the same location). In Figures 6*a* and 6*b*, the dotted lines denote the low-resolution result for η as a function of time. For $t/P^a_{\rm rot} \lesssim 5$, the results agree well, implying that a fair qualitative convergence has been achieved. For later times, the accumulation of numerical truncation error and problems associated with the inadequate outer boundaries results in a poorer agreement between the two resolutions.

The differentially rotating ellipsoids formed after saturation are highly flattened and still seem to have high $\beta \gtrsim 0.2$. We expect these to be secularly unstable against gravitational radiation (Stergioulas & Friedman 1998). Therefore, η will probably maintain a fairly high value of $O(0.1)$ on a radiation reaction timescale, which is much longer than the rotational period. As argued by Lai & Shapiro (1995), such an ellipsoid will ultimately settle down to an axisymmetric star or a Dedekind-like ellipsoid (a nonaxisymmetric, stationary star whose figure does not rotate but which has internal differential motion; cf. Chandrasekhar 1969).

As a measure of gravitational waveforms, we show h_+ and $h_\times$[5]

$$h_+ \equiv r(\tilde{\gamma}_{xx} - \tilde{\gamma}_{yy})/2M\ , \tag{17}$$

$$h_\times \equiv r\tilde{\gamma}_{xy}/M \tag{18}$$

in Figure 9 for models D1 (*dotted lines*), D2 (*solid lines*), and D3 (*dashed lines*). These quantities are read off near the

---

[5] Our quantities h_+ and $h_\times$ differ from those defined in Misner, Thorne, & Wheeler (1973) by a factor r/M.

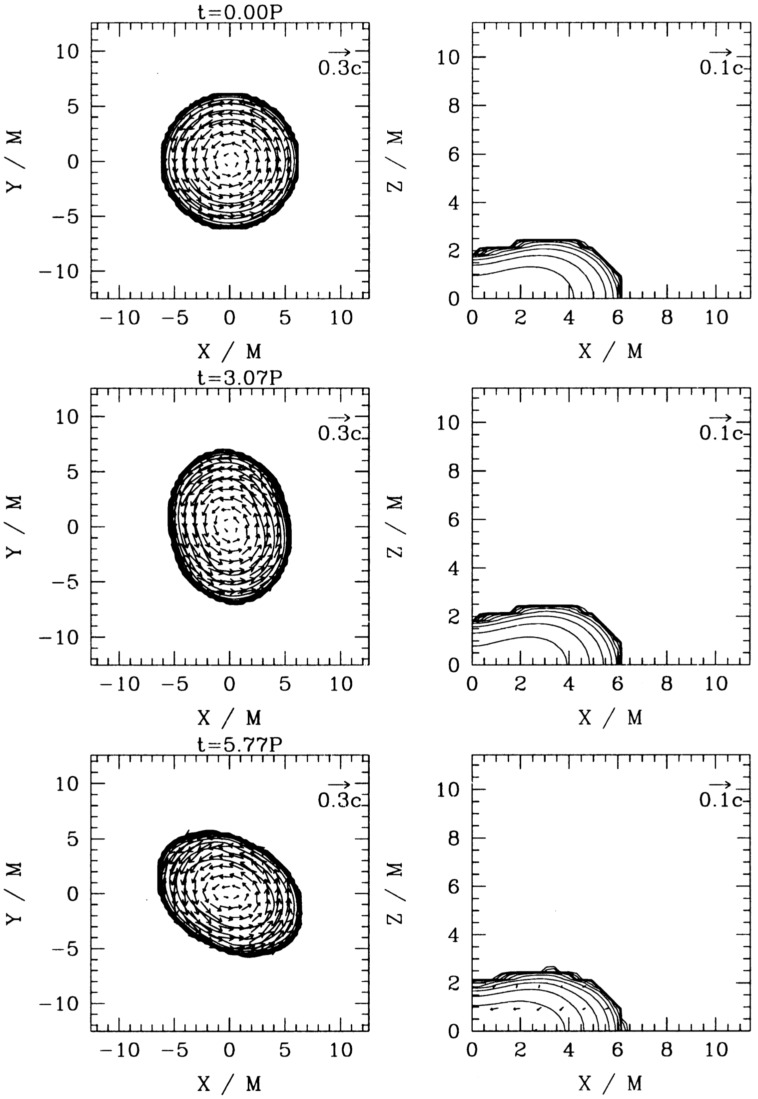

FIG. 5.—Snapshots of density contours for ρ_* and the velocity flow for v^i in the equatorial plane (*left*) and in the $y = 0$ plane (*right*) for the unstable model D3. The contour lines are drawn for $\rho_*/\rho_{*\max} = 10^{-0.3j}$ for $j = 0, 1, 2, \ldots, 10$, where $\bar{\rho}_{*\max}$ is 0.128, 0.152, and 0.176 for the three different times. The lengths of arrows are normalized to 0.3c (*left*) and 0.1c (*right*). The time is shown in units of $P^a_{\rm rot}$.

outer boundaries along the z-axis as a function of retarded time. For models D6 and D7, very similar waveforms to those of D2 and D3 are generated, as expected from Figure 6. As mentioned above, the outer boundaries are not located in the wave zone, which implies that these quantities will not exactly agree with the asymptotic waveforms. We guess that the wave shapes are in fairly good agreement with the exact ones because the frequency agrees with the oscillation frequency of the bar pattern, but the error in the amplitude may be $\gtrsim 10\%$.

We find that for unstable stars the maximum magnitude of h_+ and $h_\times$ is $\sim$0.03–0.08 depending on β and R/M, while they remain of $O(10^{-3})$ for the stable star D1. The maximum observable wave amplitude from such a source situated at a distance r from the Earth is then approximately

$$h \sim 6 \times 10^{-22}\left(\frac{h_{+,\times}}{0.05}\right)\left(\frac{M}{2.5\ M_\odot}\right)\left(\frac{10\ \text{Mpc}}{r}\right). \qquad (19)$$

The typical gravitational wavelength after saturation is $\sim 1.3P^a_{\rm rot}$ or, using the empirical relation $P^a_{\rm rot} \sim 3M(R/M)^{3/2}$ (cf. Table 1), approximately $70M(R/7M)^{3/2}$. This implies that the frequency of gravitational waves is

$$f \sim 1.2\left(\frac{R}{7M}\right)^{-3/2}\left(\frac{2.5\ M_\odot}{M}\right)\ \text{kHz}\ . \qquad (20)$$

We note that the amplitude and frequency are in approximate agreement with earlier Newtonian calculations (Houser et al. 1994; Smith et al. 1996; Houser & Centrella 1996), which suggests that GR effects do not drastically alter the simple quadrupole-formula predictions for the waveforms.

Equations (19) and (20) give the maximum amplitude for one cycle and its frequency. As discussed in Lai & Shapiro (1995), the effective amplitude can be much larger because of the quasi-periodic nature of the source. Also, the frequency will gradually shift to smaller values as a result of radiation reaction. Thus, even if h in one cycle is small and the frequency is initially as high as $\gtrsim 1$ kHz, these nearly ellipsoidal stars may eventually be observable by kilometer-size laser-interferometric gravitational wave detectors like LIGO (Thorne 1995) for stars with $M \sim 2.5\ M_\odot$ and

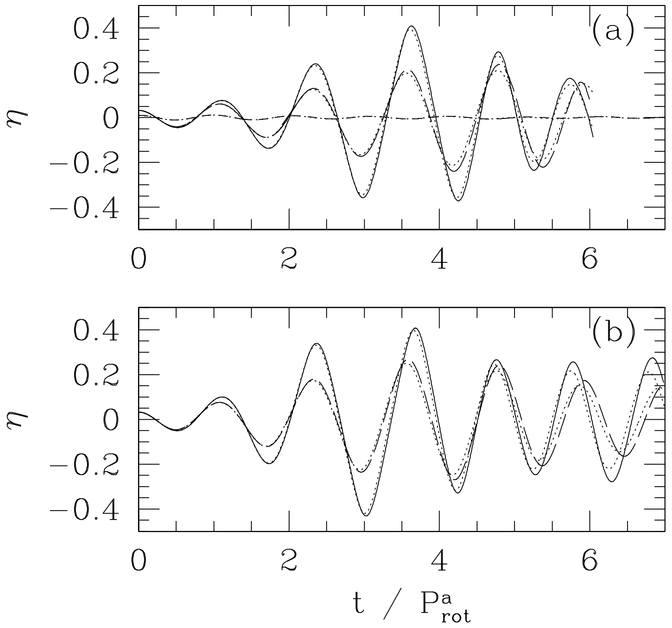

FIG. 6.—Distortion parameter η as a function of t for models (*a*) D1 (*dashed line*), D2 (*solid line*), and D3 (*long-dashed line*) and (*b*) D6 (*solid line*) and D7 (*long-dashed line*). The results in a low-resolution simulation with $101 \times 51 \times 51$ grid points are shown by the dotted lines.

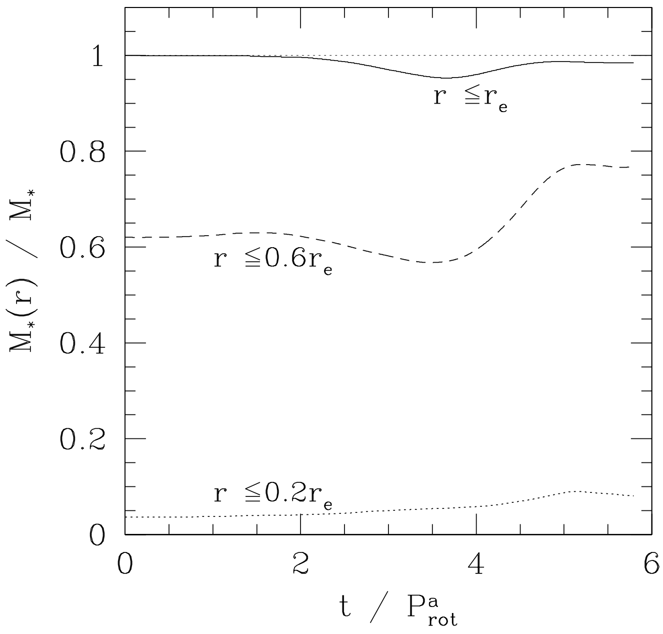

FIG. 8.—Fraction of the rest mass inside a coordinate radius as a function of t for the unstable model D2.

$R \sim 7M$ as a result of the secular decrease of the frequency. Clearly, this predicted drift needs to be confirmed by a more detailed study. Also, gravitational waves could be a source for specially designed narrowband interferometers or resonant-mass detectors in which the frequency band is between 1 and 2 kHz (Thorne 1995).

5. SUMMARY

We have performed numerical simulations of rapidly and differentially rotating neutron stars in full 3 + 1 general relativity. We treated compact stars of $10 \gtrsim R/M \gtrsim 6$ and focused on their dynamical stability against bar-mode formation. We found that when plotted in an $\bar{M}_0$ versus $\bar{\rho}_{\rm max}$ diagram a region of stable stars can be clearly distinguished from a region of unstable stars, with the onset of instability almost independent of the degree of differential rotation. We showed that the parameter $\beta = T/W$ remains a good diagnostic of the onset point of instability in the relativistic domain as it did for Newtonian stars. The critical value for the instability onset depends only weakly on the degree of differential rotation for the models surveyed to date. For those cases, we find that $\beta_{\rm dGR} \sim 0.24$–$0.25$ and that $\beta_{\rm dGR}$ decreases slightly for stars with a higher degree of differential rotation. We also have preliminary evidence that $\beta_{\rm dGR}$

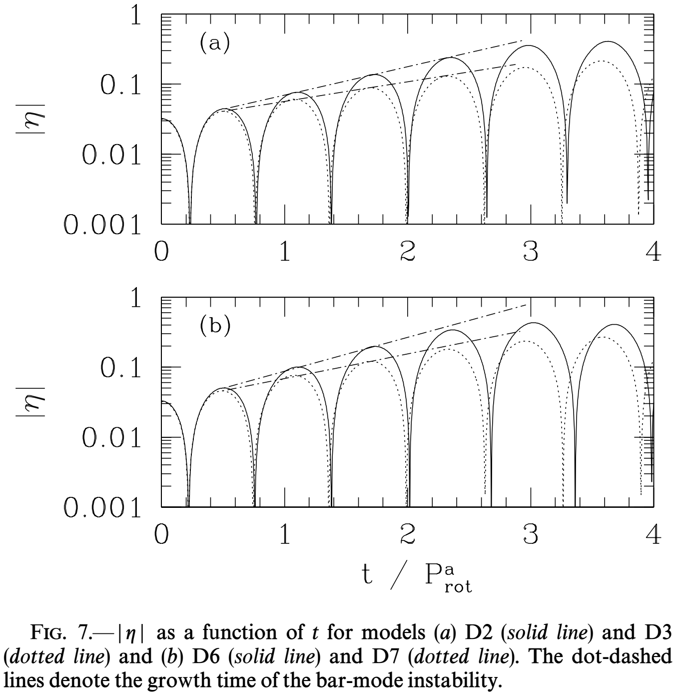

FIG. 7.—$|\eta|$ as a function of t for models (*a*) D2 (*solid line*) and D3 (*dotted line*) and (*b*) D6 (*solid line*) and D7 (*dotted line*). The dot-dashed lines denote the growth time of the bar-mode instability.

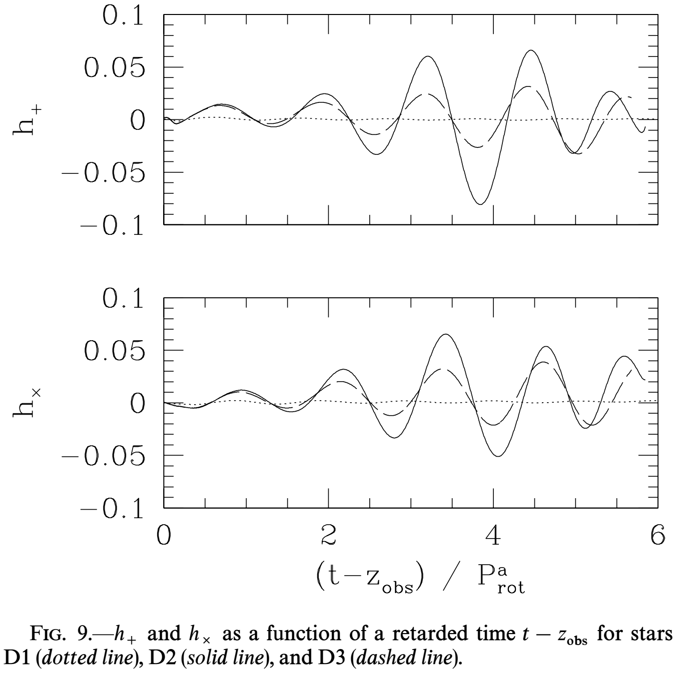

FIG. 9.—h_+ and $h_\times$ as a function of a retarded time $t - z_{\rm obs}$ for stars D1 (*dotted line*), D2 (*solid line*), and D3 (*dashed line*).

decreases with compaction as well. We will systematically study this hypothesis with a post-Newtonian numerical analysis in a forthcoming paper (Saijo et al. 2000).

For selected models, we followed the growth and saturation of bar-mode perturbations up to late times. Stars with sufficiently large $\beta > \beta_{\rm dGR}$ develop bars first and then form spiral arms, leading to mass ejection. Stars with smaller values of $\beta \sim \beta_{\rm dGR}$ also develop bars but do not form spiral arms and eject only very little mass. In both cases, unstable stars appear to form differentially rotating, triaxial ellipsoids once the bar-mode perturbation saturates. Typically, these flattened ellipsoids appear to have $\beta \gtrsim 0.2$, so that they would be secularly unstable due to gravitational waves and viscosity. We expect that this secular instability will allow the stars to maintain a barlike shape for many dynamical timescales, leading to quasi-periodic emission of gravitational waves.

We estimate the initial frequency and amplitude of gravitational waves to be $f \sim$ 1–1.4 kHz and $h \sim 5 \times 10^{-22}$ for stars of mass $\sim 2.5\, M_\odot$ and radius $R \sim 7M$ at a distance of 10 Mpc. The effective amplitude of gravitational waves could be much larger during the subsequent evolution because of the accumulation of quasi-periodic wave cycles (Lai & Shapiro 1995). In order to accurately determine the secular evolution of the ellipsoidal star together with emitted gravitational wave signal, a more detailed calculation is necessary. Since the secular timescale is larger than the dynamical timescale by several orders of magnitude, it may be impossible to follow the evolution with a fully dynamical code, even with implicit differencing to avoid the Courant criterion for stability. This suggests that in full GR, the secular evolution problem may best be solved within an appropriate, quasi-stationary scheme similar in spirit to the approach used in stellar evolution calculations.

Numerical computations were performed on the VX/4R machines in the data processing center of the National Astronomical Observatory of Japan. This work was supported by NSF grants AST 96-18524 and PHY 99-02833 and NASA grant NAG 5-7152 at the University of Illinois at Urbana-Champaign (UIUC). M. S. gratefully acknowledges support by JSPS (Fellowships for Research Abroad) and the hospitality of the Department of Physics at UIUC.

REFERENCES

Abrahams, A. M., et al. 1998, Phys. Rev. Lett., 80, 1812

Arnowitt, R., Deser, S., & Misner, C. W. 1962, in Gravitation: An Introduction to Current Research, ed. L. Witten (New York: Wiley)

Asada, H., & Shibata, M. 1996, Phys. Rev. D, 54, 4944

Baumgarte, T. W., & Shapiro, S. L. 1999, Phys. Rev. D, 59, 024007

Baumgarte, T. W., Shapiro, S. L., & Shibata, M. 2000, ApJ, 528, L29

Bishop, N., Gomez, R., Lehner, L., Szilagyi, B., Winicour, J., & Isaacson, R. 1996, Phys. Rev. Lett., 76, 4303

Bonazzola, S., Frieben, J., & Gourgoulhon, E. 1996, ApJ, 460, 379

Bonazzola, S., Gourgoulhon, E., Salgado, M., & Marck, J. A. 1993, A&A, 278, 421

Bonazzola, S., & Marck, J. A. 1993, A&A, 267, 623

Bowen, J., & York, J. W., Jr. 1980, Phys. Rev. D, 21, 2047

Chandrasekhar, S. 1969, Ellipsoidal Figures of Equilibrium (New Haven: Yale Univ. Press)

Cook, G. B., Shapiro, S. L., & Teukolsky, S. A. 1992, ApJ, 398, 203

———. 1994, ApJ, 422, 227

———. 1996, Phys. Rev. D, 53, 5533

Cutler, C., & Lindblom, L. 1992, ApJ, 385, 630

Durisen, R. H., Gingold, R. A., Tohline, J. E., & Boss, A. P. 1986, ApJ, 305, 281

Friedman, J. L., & Schutz, B. F. 1978, ApJ, 222, 281

Goussard, J. O., Haensel, P., & Zdunik, J. L. 1998, A&A, 330, 1005

Hawley, J. F., Smarr, L. L., & Wilson, J. M. 1984, ApJS, 55, 211

Houser, J. L., & Centrella, J. M. 1996, Phys. Rev. D, 54, 7278

Houser, J. L., Centrella, J. M., & Smith, S. 1994, Phys. Rev. Lett., 72, 1314

Imamura, J. N., Friedman, J. L., & Durisen, R. H. 1985, ApJ, 294, 474

Imamura, J. N., Toman, J., Durisen, R. H., Pickett, B. K., & Yang, S. 1995, ApJ, 444, 363

Ipser, J. R., & Lindblom, L. 1990, ApJ, 355, 226

Kaspi, V. M., et al. 1998, ApJ, 503, L161

Kley, W., & Schäfer, G. 1999, Phys. Rev. D, 60, 027501

Komatsu, H., Eriguchi, Y., & Hachisu, I. 1989a, MNRAS, 237, 355

———. 1989b, MNRAS, 239, 153

Lai, D., & Shapiro, S. L. 1995, ApJ, 442, 259

Lynden-Bell, D., & Ostriker, J. P. 1967, MNRAS, 136, 293

Marshall, F. E., et al. 1998, ApJ, 499, L179

Misner, C. W., Thorne, K. S., & Wheeler, J. A. 1973, Gravitation (San Francisco: Freeman)

New, K. C. B., Centrella, J. M., & Tohline, J. E. 2000, Phys. Rev. D, in press

Oohara, K., & Nakamura, T. 1999, Prog. Theor. Phys. Suppl., 136, 270

Ostriker, J. P., & Bodenheimer, P. 1973, ApJ, 180, 171

Pickett, B. K., Durisen, R. H., & Davis, G. A. 1996, ApJ, 458, 714

Rampp, M., Müller, E., & Ruffert, M. 1998, A&A, 332, 969

Saijo, M., Shibata, M., Baumgarte, T. W., & Shapiro, S. L. 2000, ApJ, submitted

Salgado, M., Bonazzola, S., Gourgoulhon, E., & Haensel, P. 1994, A&A, 291, 155

Shapiro, S. L., & Teukolsky, S. A. 1983, Black Holes, White Dwarfs, and Neutron Stars (New York: Wiley)

Shapiro, S. L., & Zane, S. 1998, ApJS, 117, 531

Shibata, M. 1999a, Phys. Rev. D, 60, 104052

———. 1999b, Prog. Theor. Phys., 101, 1199

Shibata, M., Baumgarte, T. W., & Shapiro, S. L. 1998, Phys. Rev. D, 58, 023002

———. 2000, Phys. Rev. D, 61, 044012

Shibata, M., & Nakamura, T. 1995, Phys. Rev. D, 52, 5428

Shibata, M., Oohara, K.-I., & Nakamura, T. 1997, Prog. Theor. Phys., 98, 1081

Shibata, M., & Uryu, K. 2000, Phys. Rev. D, 61, 064001

Smith, S., Houser, J., & Centrella, J. M. 1996, ApJ, 458, 236

Stergioulas, N., & Friedman, J. L. 1998, ApJ, 492, 301

Tassoul, J. 1978, Theory of Rotating Stars (Princeton: Princeton Univ. Press)

Thorne, K. S. 1995, in Particle and Nuclear Astrophysics and Cosmology in the Next Millennium, ed. E. W. Kolb & R. Peccei (Singapore: World Scientific), 398

Tohline, J. E., Durisen, R. H., & McCollough, M. 1985, ApJ, 298, 220

Tohline, J. E., & Hachisu, I. 1990, ApJ, 361, 394

Torii, K., et al. 1999, ApJ, 523, L69

van Leer, B. J. 1977, J. Comput. Phys., 23, 276

Williams, H. A., & Tohline, J. E. 1987, ApJ, 315, 594

———. 1988, ApJ, 334, 449

Yoshida, S., & Eriguchi, Y. 1999, ApJ, 515, 414